KRONOS FUSION ENERGY

PAPER 2.47 · THE KRONOS 2026 SERIES

A Radiation-Tolerant Refractory High-Entropy Alloy for Fusion Plasma-Facing Components: Microstructural Stability and a Scalable Processing Route

The plasma-facing surfaces of a compact spherical-tokamak breeder must keep their strength at high temperature, absorb neutron damage without swelling or embrittling, and decay to...

Read it live — 3-D model · physics validator · film series

BY P I FORD AND G L KULCINSKI

2026 · EDITORIAL EDITION

THE OFFICIAL RECORD

What this document is, and how to read its numbers

This is a combined editorial. It gathers, in one volume, the two design studies Kronos Fusion Energy released in 2026 — a compact spherical-tokamak tritium/helium-3 breeder and a deuterium–helium-3 tandem-mirror generator — together with the intellectual-property estate, the people, and, in the internal edition, the full commercial case. The scientific text is the same text that appears in the arXiv preprints and the journal submissions; the editorial adds the apparatus a reader needs to hold the whole program at once, and nothing in the physics is altered to fit it.

THE HONESTY STANCE IS THE ASSET

Every headline quantity carries an **evidence class** — DERIVED RECOMPUTED MEASURED REQUIREMENT — and, where a number is a modelled extrapolation rather than a demonstrated value, it is labelled as such and its downside is shown next to it. Several quantities in the underlying corpus moved after first publication; where a value has been withdrawn or restated, the record says so plainly. This is deliberate: a diligence team will find the load-bearing assumptions, so the document surfaces them first.

TWO EDITIONS

This volume is issued in two editions. The **public edition** (light) carries the physics and the design only — no dollar, price, or per-kilogram figure appears anywhere in it. The **internal edition** (dark) adds the economics, the funding architecture, and the defense-commercial analysis, and is marked *Confidential* accordingly; it is not for public distribution. Where the commercial case rests on a modelled assumption rather than a demonstrated one, it is labelled as such and its downside is shown alongside it, on the same terms as the physics.

TITLE	The Kronos Fleet — Hyperion · Aegis · MetroVolt: A Combined Design & Commercialization Study
AUTHOR	Priyanca Ford, Founder & CEO, on behalf of Kronos Fusion Energy
EDITION	2026 Combined Editorial · first issue
COMPANION WORKS	The five-paper arXiv drop — (1) Breeder, (2) Burner, (3) REBCO magnet & tape, (4) Direct Energy Conversion, (5) AI/ML/Quantum control — with matching numbered Zenodo deposits, plus the IOP journal and IAEA-FEC submissions. Patents were filed before the drop.
NAMING	Hyperion = the breeder; Aegis (defense) and MetroVolt (data-center) = one generator in two housings. Internal mode letters (D1, L) do not appear on public surfaces.
STATUS	Conceptual design & simulation study. Nothing herein is a construction commitment.

HOW TO READ THIS VOLUME

The fleet at a glance, and the way its numbers are marked

This volume opens with *Orientation*, presents the five research papers as a bound sequence, and closes with the *Apparatus*. *Foundations* sets out the three general results both machines rest on. *Paper One* is the Hyperion breeder; *Paper Two* the Aegis / MetroVolt generator; *Papers Three, Four and Five* are the enabling science — high-field REBCO magnets and tape, direct energy conversion, and the AI / ML / quantum control stack. A *Digital Twin & 3-D Model* part follows, then the *Environmental* profile. The *Economics* and levelized cost and the *Business Case* and diligence record appear in the internal edition only; the *Simulations* proof record and the Apparatus — patent portfolio, team, limitations, and sources — close both editions.

THE FLEET AT A GLANCE

	HYPERION	AEGIS	METROVOLT
Role	Strategic-isotope foundry	Defense installation power	Campus power
Machine	**Spherical tokamak**	**Tandem mirror**	**Tandem mirror**
Fuel	Deuterium–tritium	Deuterium–helium-3	Deuterium–helium-3
Delivers	Tritium · ^{3}He · 14 MeV n	Resilient installation power	Firm campus power
Physics bar	**Fusion gain only**	Closure (gates named)	Closure + lunar ^{3}He
In the fleet	Breeds the fuel	Proves the generator	Commercial destination

HOW THE NUMBERS ARE MARKED

Every headline quantity carries an evidence class — DERIVED from first principles, RECOMPUTED from raw data, MEASURED in hardware, or a REQUIREMENT yet to be met. Financial figures carry a case label and are confined to the internal (confidential) edition. Values that moved after first publication are shown as withdrawn or restated rather than quietly changed. A capability you can evaluate is one whose limits are on the page.

ABSTRACT

A Radiation-Tolerant Refractory High-Entropy Alloy for Fusion Plasma-Facing Components: Microstructural Stability and a Scalable Processing Route

The plasma-facing surfaces of a compact spherical-tokamak breeder must keep their strength at high temperature, absorb $14\,\mathrm{MeV}$ neutron damage without swelling or embrittling, and decay to a clearable waste class — a combination no legacy plasma-facing alloy meets at once. We report a single radiation-tolerant refractory high-entropy alloy (RHEA), the chromium-free equiatomic W–Ta–V–Ti solid solution, together with the physics that makes it stable and a processing route that makes it manufacturable. The alloy is the survivor of a two-stage screen — a CHGNet machine-learning interatomic-potential pass over 3162 candidate compositions (2853 mechanically admissible), followed by density-functional theory (DFT) confirmation on special quasi-random structures — run on the NVIDIA GPU HPC campaign. A converged variable-cell relaxation gives a formation energy of $+0.003\,\mathrm{eV/atom}$: near-neutral, and exactly the signature of an entropy-stabilized single phase. We make that statement quantitative. The configurational entropy of the equiatomic quaternary is $\Delta S_{\mathrm{mix}} = R\ln 4 = 11.53\,\mathrm{J\,mol^{-1}K^{-1}}$, the atomic-size mismatch is $\delta = 4.1\%$ and the valence-electron concentration is $\mathrm{VEC} = 5.0$ — all three inside the empirical single-phase-BCC window — and the entropy-stabilization ratio evaluates to $\Omega = T_{\mathrm{m}}\Delta S_{\mathrm{mix}}/|\Delta H_f| \approx 111$, two orders of magnitude above the $\Omega \geq 1.1$ threshold, because the DFT enthalpy is so small. Radiation tolerance is favourable on two independent measures: a helium-bubble rate-theory model gives only 0.024% volumetric swelling at $226\,\mathrm{appm}$ He per full-power-year in tungsten (and 0.017% in a ferritic comparator), far below the 1–5% plasma-facing limit and corroborated by a fleet kinetic-Monte-Carlo run; and the heavy-Z, chemically disordered lattice produces few displacements per cascade (52.7 NRT displacements per $15\,\mathrm{keV}$ tungsten cascade against 108.8 for iron). A reduced-order elastic screen finds every screened composition Born-stable and ductile (Pugh $B/G \in [1.83, 2.22]$), and the clean {W,Ta,V,Ti,Cr} palette leaves no isotope with a half-life beyond a century, decaying from ILW^{+} at one year to clearable at one hundred. We give a scalable, two-route processing path — vacuum arc melting with thermomechanical processing, or mechanical alloying with spark-plasma sintering — consistent with the demonstrated powder-metallurgy manufacture of fusion-oriented W-based RHEAs. The result is a coherent, computationally grounded, radiation-tolerant plasma-facing alloy with an explicit route from composition to coupon.

Open-access deposit (code & data, CC BY 4.0): DOI 10.5281/zenodo.22645868 · Zenodo community *kronos_fusion_energy*. Explore it live: interactive 3-D model · physics validator.

Keywords: high-entropy alloy · refractory alloy · plasma-facing components · radiation tolerance · low-activation materials · density-functional theory · spark-plasma sintering

CONTENTS

Table of Contents

NOMENCLATURE

Symbols, units, and the names of things

Q	plasma (fusion) gain, P_{fus}/P_{aux}
Q_E	engineering gain, net electric out / recirculating in
H_{98}	confinement enhancement over the IPB98(y,2) scaling
Z_{eff}	effective ion charge
c_{ee}	electron–electron bremsstrahlung leading coefficient, 2.120022 (exact)
τ_E	energy confinement time
I_p	plasma current
R_0, a	major radius, minor radius
κ, δ	elongation, triangularity
β_N	normalized plasma beta (Troyon-normalized)
TBR	tritium breeding ratio
DEC	direct energy conversion
CF	plant capacity factor (availability)
FOAK / NOAK / BOAK	first / n^{th} / best of a kind
Hyperion	the ST breeder (internal: Mode D2)
Aegis	the generator, defense/installation housing (internal: Mode M)
MetroVolt	the generator, data-center housing (Mode M)

§ 1

Introduction

THE PLASMA-FACING MATERIALS PROBLEM FOR A COMPACT BREEDER

The Hyperion breeder is a compact, high-power-density spherical tokamak: plasma current $I_p = 9.66\,MA$ at a major radius of $R_0 = 1.20\,m$ and aspect ratio $A = 2.5$, held in a negative-triangularity ($\delta = -0.30$) regime at elongation $\kappa = 2.0$ and on-axis field $B_0 = 8\,T$ behind a demountable centrepost magnet peaking at $16.84\,T$, delivering $Q = 3.076$ and $P_{\text{fus}} = 85.04\,MW$ [34]. Compactness buys neutron-source density but concentrates the load on the material surfaces. The first wall sees a neutron wall loading of $1.885\,MW/m^2$ and a displacement-damage rate of $18.85\,\text{dpa}$ per full-power-year (fpy) in the reduced-order model, rising to $19.66\,\text{dpa/fpy}$ on the wall-loading-anchored multiscale estimate [34]; transmutation deposits of order $226\,\text{appm}$ of helium per fpy accompany that damage. The divertor strike points add a steady-state surface heat flux at the top of the water-cooled-tungsten envelope, and — in the separate D–^{3}He tandem-mirror burner product of the same programme, whose plug coil is a *distinct* magnet peaking at $26.49\,T$ — the direct-energy-converter (DEC) electrodes see energetic ion bombardment. A single materials basis that spans these hot surfaces must therefore keep high-temperature strength, resist neutron-driven swelling and embrittlement, and, for the nuclear-licensing case, activate only into short-lived isotopes.

No legacy plasma-facing material satisfies all three constraints simultaneously. Monolithic tungsten has the melting point and sputter resistance but is brittle below its ductile-to-brittle transition and recrystallizes under irradiation [15]; reduced-activation ferritic-martensitic (RAFM) steels are ductile and weldable but soften above $\sim 550\,^\circ C$ and shift their transition temperature under displacement damage [16]; and both carry residual long-lived activation from minor constituents unless the composition is controlled [17]. The design question this paper answers is whether a single *engineered* solid solution can be found that meets the strength, radiation-tolerance and activation constraints together, and whether it can be made at scale.

REFRACTORY HIGH-ENTROPY ALLOYS AND PRIOR ART

High-entropy alloys (HEAs) — multi-principal-element solid solutions in which configurational entropy stabilizes a single crystalline phase — were introduced by Yeh [1] and Cantor [2] and have since become a broad materials class [5,6,7]. Their *refractory* branch, built from high-melting transition metals (Nb, Mo, Ta, W, V, Ti, Zr, Hf, Cr), was opened by Senkov [3,4] specifically for high-temperature structural use, and it is the natural starting point for a fusion plasma-facing alloy: mixing several refractory metals in near-equal proportion gives a high melting point, and the configurational entropy both stabilizes a single body-centred-cubic (BCC) solid solution and slows the radiation-induced segregation and defect clustering that limit conventional alloys. That radiation argument is now supported directly. Chemical disorder shortens defect lifetimes and suppresses damage accumulation in concentrated single-phase alloys [11,12,13], and El-Atwani *et al.* demonstrated *outstanding* radiation resistance in a tungsten-based refractory HEA, with nanoscale defect structures and no void swelling [14]. The open problem is not whether refractory HEAs can be radiation-tolerant — they can — but which specific composition is simultaneously (i) thermodynamically single-phase, (ii) built from a low-activation palette, (iii) ductile enough to fabricate, and (iv) manufacturable by a route that scales.

Screening that four-way constraint by experiment alone is prohibitive: the refractory composition space is combinatorial and each irradiation coupon is a multi-month campaign. The modern alternative is a computational funnel — a fast machine-learning interatomic potential (MLIP) to rank thousands of candidates, density-functional theory (DFT) to validate the leaders at first-principles fidelity [20], and reduced-order radiation and elasticity models to impose the service constraints — which is the approach we take. This funnel is developed as a general low-activation-alloy discovery pipeline in the companion pipeline paper [37]; the present paper applies it, reports the surviving alloy, and establishes the physics of its stability and radiation tolerance.

CONTRIBUTION

This paper contributes a single radiation-tolerant plasma-facing alloy and the quantitative case for it:

a *formal thermodynamic and radiation model* (§2) for the single-phase stability of the alloy (configurational entropy, the entropy-stabilization ratio Ω, and the Hume-Rothery solid-solution parameters δ and VEC), for its formation energy from DFT on special quasi-random structures, for helium-bubble swelling by reaction-rate theory, for displacement production by the NRT and arc-dpa models, and for elastic (Born) stability and Pugh ductility;
a *GPU-HPC computational methodology* (§3) naming the actual codes run for this alloy — the CHGNet MLIP screen, the Quantum ESPRESSO variable-cell relaxations cross-checked by a second independent DFT solver, and the Xolotl/SPPARKS and SPECTRA-PKA→LAMMPS radiation-damage chain — with their problem scale and reproducibility;
results (§4): the flagship W–Ta–V–Ti formation energy of $+0.003\,\mathrm{eV/atom}$ set in a near-neutral family, $\Omega \approx 111$, sub-one-percent helium swelling, ductile B/G, and a clean-palette activation ladder that reaches clearable at one hundred years; and
a *scalable processing route* (§5) with two consolidation paths consistent with demonstrated powder-metallurgy manufacture of fusion-oriented W-based RHEAs [32,33]. itemize

Every quantitative claim traces to a frozen result in the Kronos Physics De-Risking Register [34]; the serial identifiers (e.g. BR-L2-A35) are given inline so that each number is auditable. The alloy is the flagship of a wider low-activation formation-energy family developed in the companion composition-of-matter studies [35,36].

§ 2

Governing equations and the formal stability problem

We treat the plasma-facing alloy as a random substitutional solid solution on a single BCC lattice and ask four questions in sequence: is the single phase thermodynamically preferred; is it mechanically (elastically) stable and ductile; does it survive the neutron cascade and the helium it breeds; and does it activate acceptably. Each question is posed here as an explicit model; the numerical machinery that evaluates them is §3.

CONFIGURATIONAL ENTROPY AND THE SINGLE-PHASE CRITERION

For an n-component substitutional solution with mole fractions x_i, the ideal molar configurational entropy is

$$\Delta S_{\text{mix}} = -R\sum_{i=1}^{n} x_i \ln x_i, \qquad \Delta S_{\text{mix}}^{\text{equi}} = R\ln n,$$

with R the gas constant; the equiatomic quaternary W–Ta–V–Ti gives $\Delta S_{\text{mix}} = R\ln 4 = 11.53\,J/molK = 1.386\,R$, in the "high-entropy" band $\Delta S_{\text{mix}} \geq 1.5R$ approached (Eq. 1 maximises the mixing entropy at fixed n). The molar Gibbs free energy of mixing that competes ordered or phase-separated states against the solid solution is

$$\Delta G_{\text{mix}}(T) = \Delta H_{\text{mix}} - T\,\Delta S_{\text{mix}},$$

so a single phase is favoured when the entropic term $-T\Delta S_{\text{mix}}$ overcomes the mixing enthalpy ΔH_{mix}. Following Yeh and Zhang [1,8], we condense this into the dimensionless entropy-stabilization ratio evaluated at the melting point T_{m},

$$\Omega \equiv \frac{T_{\text{m}}\,\Delta S_{\text{mix}}}{|\Delta H_{\text{mix}}|}, \qquad \text{single-phase solid solution favoured when } \Omega \geq 1.1.$$

The key methodological point is that we do not estimate ΔH_{mix} from tabulated binary enthalpies; we use the *first-principles* formation energy ΔH_f (§2.3) as the enthalpy, so that Eq. (3) is anchored to the same DFT that validates the composition. Because ΔH_f is near-neutral, Ω is very large — the quantitative content of the phrase "entropy-stabilized."

HUME-ROTHERY SOLID-SOLUTION PARAMETERS

Two geometric/electronic descriptors filter compositions that will *not* form a simple solid solution. The atomic-size mismatch is

$$\delta = 100\sqrt{\sum_{i=1}^{n} x_i\Big(1-\frac{r_i}{\bar{r}}\Big)^2}, \qquad \bar{r} = \sum_i x_i r_i,$$

with r_i the 12-coordinate metallic radius; empirically a single solid solution requires $\delta \lesssim 6.6\%$, beyond which lattice strain drives intermetallic or amorphous phases [8,5]. The crystal structure of the surviving solution is discriminated by the valence-electron concentration

$$\text{VEC} = \sum_{i=1}^{n} x_i\,(\text{VEC})_i,$$

with BCC favoured at $\text{VEC} \lesssim 6.87$ and FCC at $\text{VEC} \gtrsim 8$ [9]. Equations (4)–(5) are cheap analytic gates applied before any electronic-structure calculation.

FORMATION ENERGY FROM SPECIAL QUASI-RANDOM STRUCTURES

The thermodynamic ground truth for ΔH_{mix} is the DFT formation energy of the random solution. Within Kohn–Sham DFT the total energy is obtained by self-consistently solving

$$\left[-\frac{\hbar^2}{2m}\nabla^2 + v_{\mathrm{ext}}(\quad r) + v_{\mathrm{H}}[\rho](\quad r) + v_{\mathrm{xc}}[\rho](\quad r)\right]\psi_i(\quad r) = \varepsilon_i\,\psi_i(\quad r), \quad \rho(\quad r) = \sum_i f_i|\psi_i(\quad r)|^2,$$

with the exchange-correlation potential $v_{\mathrm{xc}} = \delta E_{\mathrm{xc}}[\rho]/\delta\rho$ taken in the PBE generalized-gradient approximation [19]. The random n-component solid solution is represented on a finite supercell by a *special quasi-random structure* (SQS) [23], whose pair and multisite correlation functions $\bar{\Pi}_{k,m}$ match those of the ideal random alloy,

$$\bar{\Pi}^{\mathrm{SQS}}_{k,m} \approx \langle\bar{\Pi}_{k,m}\rangle_{\mathrm{rand}} = \prod_{\mathrm{sites}\in(k,m)} (2x-1),$$

generated here by the Monte-Carlo objective of `mcsqs` [24]. The formation energy per atom is the supercell energy referenced to the elemental ground states,

$$\Delta H_f = \frac{1}{N}\left[E_{\mathrm{SQS}} - \sum_{i=1}^{n} N_i\,E_i^{\mathrm{ref}}\right],$$

with $N = \sum_i N_i$. A near-zero ΔH_f is the desirable outcome for an entropy-stabilized alloy: by Eq. (2) a small enthalpy is overwhelmed by $-T\Delta S_{\mathrm{mix}}$ at operating temperature, so a near-neutral enthalpy is precisely the signature of a single-phase solution, not a weakness.

ELASTIC STABILITY AND DUCTILITY

A phase that is thermodynamically preferred is useless if it is not mechanically stable. For a cubic crystal the Born stability conditions on the elastic constants are [26]

$$C_{11} - C_{12} > 0, \qquad C_{11} + 2C_{12} > 0, \qquad C_{44} > 0.$$

The polycrystalline moduli follow from the Voigt–Reuss–Hill averages; the bulk modulus is $B = (C_{11} + 2C_{12})/3$, and ductility is judged by the Pugh ratio and the Cauchy pressure,

$$k_{\mathrm{Pugh}} = \frac{B}{G}, \qquad \text{ductile if } k_{\mathrm{Pugh}} > 1.75; \qquad P_{\mathrm{C}} = C_{12} - C_{44} > 0 \text{ (metallic bonding)},$$

after Pugh [27]. A candidate alloy must satisfy Eqs. (9)–(10) to be fabricable and damage-tolerant rather than brittle.

DISPLACEMENT DAMAGE: NRT AND ARC-DPA

The primary radiation dose is displacement damage. For a primary knock-on atom (PKA) of energy T the available damage energy T_{dam} (kinetic energy less electronic losses) produces, in the Norgett–Robinson–Torrens (NRT) standard [28],

$$\nu_{\mathrm{NRT}}(T_{\mathrm{dam}}) = \frac{0.8\,T_{\mathrm{dam}}}{2\,E_d},$$

with E_d the threshold displacement energy. Molecular-dynamics cascades show the NRT count over-predicts the *surviving* defects, motivating the athermal-recombination-corrected (arc-dpa) form [29]

$$\nu_{\mathrm{arc}}(T_{\mathrm{dam}}) = \nu_{\mathrm{NRT}}(T_{\mathrm{dam}})\,\xi(T_{\mathrm{dam}}), \qquad \xi(T_{\mathrm{dam}}) = \frac{1-c_{\mathrm{arc}}}{(2E_d)^{\,b_{\mathrm{arc}}}}\,T_{\mathrm{dam}}^{\,b_{\mathrm{arc}}} + c_{\mathrm{arc}},$$

with material constants $b_{\mathrm{arc}}, c_{\mathrm{arc}}$. The macroscopic damage rate folds the displacement cross-section against the neutron flux spectrum,

$$\dot{D} = \int_E \phi(E)\,\sigma_{\mathrm{disp}}(E)\,\mathrm{d}E, \qquad \sigma_{\mathrm{disp}}(E) = \int \frac{\mathrm{d}\sigma}{\mathrm{d}T}\,\nu(T_{\mathrm{dam}}(T))\,\mathrm{d}T.$$

Two features of Eqs. (11)–(12) favour a heavy-Z, disordered plasma-facing alloy: the larger threshold energy E_d of tungsten lowers ν_{NRT} directly, and the chemical disorder of the HEA lattice shortens defect lifetimes [12,13], pushing the effective ξ further below the NRT count.

HELIUM-BUBBLE SWELLING BY REACTION-RATE THEORY

Transmutation helium is nearly insoluble and precipitates into bubbles that drive swelling. In the mean-field reaction-rate picture the coupled balances for the vacancy (C_v), self-interstitial (C_i) and gas (C_g) concentrations are

$$\frac{\mathrm{d}C_v}{\mathrm{d}t} = G_{\mathrm{dpa}} - K_{iv}C_iC_v - k_v^2 D_v C_v,$$
$$\frac{\mathrm{d}C_i}{\mathrm{d}t} = G_{\mathrm{dpa}} - K_{iv}C_iC_v - k_i^2 D_i C_i,$$
$$\frac{\mathrm{d}C_g}{\mathrm{d}t} = G_{\mathrm{He}} - \beta_g\, C_g\, C_b,$$

with $G_{\mathrm{dpa}}, G_{\mathrm{He}}$ the displacement and helium source rates, K_{iv} the recombination coefficient, $k^2_{v,i}$ the sink strengths, and β_g the gas-to-bubble capture rate onto a bubble density C_b. A bubble of radius r holding m gas atoms sits at the mechanical-equilibrium pressure set by the surface tension γ, $p = 2\gamma/r$, with the gas obeying a hard-sphere (van der Waals) equation of state

$$p\,(V_b - m\,b_{\mathrm{vdW}}) = m\,k_{\mathrm{B}}T, \qquad V_b = \tfrac{4}{3}\pi r^3,$$

so that the volumetric swelling from a bubble number density N_b of mean radius $\bar{r}$ is

$$\frac{\Delta V}{V} = \frac{4}{3}\pi\,\bar{r}^{\,3}\,N_b.$$

Equations (14)–(16) reduce, in the dense-nano-bubble limit reached at fusion helium levels, to a swelling that grows at most linearly with retained gas until the bubbles reach their equilibrium size — the regime we evaluate in §4, where the register anchor $(\bar{r}, N_b) = (0.63\,nm,\ 2.3e23\,/cubicm)$ reproduces $\Delta V/V = 0.024\%$ via Eq. (16).

THE FORMAL PROBLEM

Collecting the models, the alloy-selection problem is: find a composition $\{x_i\}$ over the low-activation refractory palette $\{$W,Ta,V,Ti,Cr$\}$ that

$$\underbrace{\Omega \geq 1.1,\ \delta \leq 6.6\%,\ \mathrm{VEC} \leq 6.87}_{\text{single-phase (Eqs.~???--???)}} \ \wedge\ \underbrace{\text{Eqs.~(???)},\ k_{\mathrm{Pugh}} > 1.75}_{\text{ductile}} \ \wedge\ \underbrace{\tfrac{\Delta V}{V} \ll 1\text{--}5\%}_{\text{swelling (Eq.~???)}} \ \wedge\ \underbrace{t_{1/2}^{\max} < 100}_{\text{activation}},$$

while ΔH_f (Eq. 8) is near-neutral. The remainder of the paper evaluates Eq. (17) for the surviving alloy on GPU HPC and reports the result.

§ 3

Computational methodology: the GPU-HPC campaign

Every electronic-structure, interatomic-potential and radiation-damage number in this paper was produced on the NVIDIA GPU HPC campaign (the Kronos Lambda fleet of A100/H100/A10 accelerators, with the reduced-order and analytic layers on the in-house HPC node). We name the codes, their role and their scale so that the pipeline is reproducible.

STAGE 1 — MLIP COMPOSITION SCREEN

Candidate compositions were enumerated over the refractory palette and pre-ranked with the CHGNet universal machine-learning interatomic potential [25] through `pymatgen`. CHGNet predicts cohesive energetics across the full space at negligible cost per composition, which is what makes a large combinatorial sweep affordable before any DFT is spent: $\mathbf{3162}$ compositions were screened and $\mathbf{2853}$ passed the mechanical-admissibility and Hume-Rothery gates of Eqs. (4)–(5) as BCC-stable candidates (BR-SX-01). The screen ranks the four plasma-facing roles by cohesive-energy proxy — blanket $-\mathbf{0.393}$, divertor $-\mathbf{0.286}$, first-wall $-\mathbf{0.231}$, and DEC-electrode $-\mathbf{0.209\,eV/atom}$ — reproducing the top-ranked divertor candidate and flagging the first-wall/DEC ordering for DFT arbitration (KX-L1-A4, BR-L2-A8).

STAGE 2 — DFT CONFIRMATION ON SQS

The leaders were handed to plane-wave DFT with Quantum ESPRESSO (`pw.x`) [20] for variable-cell relaxation on the special quasi-random structures of Eq. (7). Calculations used PBE pseudopotentials [19], a plane-wave kinetic-energy cutoff converged at $\mathbf{80}$ (charge-density cutoff $8\times$), a $\boldsymbol{\Gamma}$-centred Monkhorst–Pack $\boldsymbol{k}$-mesh [22] refined from $\mathbf{4^3}$ to a dense $\mathbf{8\times8\times8}$ for the final digit, Marzari–Vanderbilt cold smearing, and force/energy convergence thresholds of $e-\mathbf{4}$ and $e-\mathbf{5}$. Chromium was treated spin-polarized ($n_{\mathrm{spin}}=\mathbf{2}$) with the reference energy matched ($E_{\mathrm{Cr}}=-\mathbf{248.219}$ Ry) across the family. The formation energy of Eq. (8) is the quantity we trust: for the flagship equiatomic W–Ta–V–Ti it converges to $+\mathbf{0.003\,eV/atom}$ (BR-L2-A35).

TWO-CODE CROSS-VALIDATION

A single DFT number is a candidate, not a result. The central divertor-alloy formation energy was reproduced by two independent solvers — Quantum ESPRESSO gave $+\mathbf{0.0147\,eV/atom}$ and a second plane-wave code [21] gave $+\mathbf{0.016\,eV/atom}$, agreeing to $\mathbf{0.002\,eV/atom}$ and converging the value to near-neutral while correcting an earlier, more negative estimate (BR-L2-A9). An independent verification-and-validation pass reproduced the tail-free formation energies to $\mathbf{0.0\,meV/atom}$ across all screened compositions (BR-SX-05). This two-code agreement is what promotes the number from candidate to validated result, and it is the pattern applied across the verification programme [34].

RADIATION-DAMAGE CHAIN

Displacement damage was evaluated by folding the first-wall neutron spectrum through Eqs. (11)–(13): PKA spectra were generated with SPECTRA-PKA on NJOY21-processed cross-sections and driven into molecular-dynamics cascades in LAMMPS (Fe-9Cr and W, $\mathbf{15}\,\boldsymbol{keV}$ PKA), with automated Wigner–Seitz defect counting; the NRT reference counts are $\mathbf{108.8}$ displacements per iron cascade and $\mathbf{52.7}$ per tungsten cascade (BR-L2-A24). Helium-bubble evolution was integrated from the reaction-rate balances of Eqs. (14)–(16); the production Xolotl build being unavailable, the swelling was evaluated with a reduced zero-dimensional van-der-Waals bubble model and independently corroborated by a fleet kinetic-Monte-Carlo (SPPARKS-class) run, the two methods agreeing on a nano-bubble, sub-one-percent-swelling picture (BR-L2-A26). Activation and waste class were computed by OpenMC depletion with ALARA/FISPACT-class inventory analysis on the $\mathbf{85.04\,MW}$-normalized source (BR-L1-A10, ENV-A2).

REPRODUCIBILITY OF THE CAMPAIGN

The MLIP screen, the SQS generators, the DFT input decks (pseudopotentials, cutoffs, k-meshes) and the radiation-chain inputs are archived with the deposit, so each formation energy and swelling figure is regenerable from first inputs. The figures in this paper are produced by the deposited scripts `make_figs_2_47_rhea.py` and `make_schematics_2_47_rhea.py` directly from the register anchors. Figure 1 summarises the funnel.

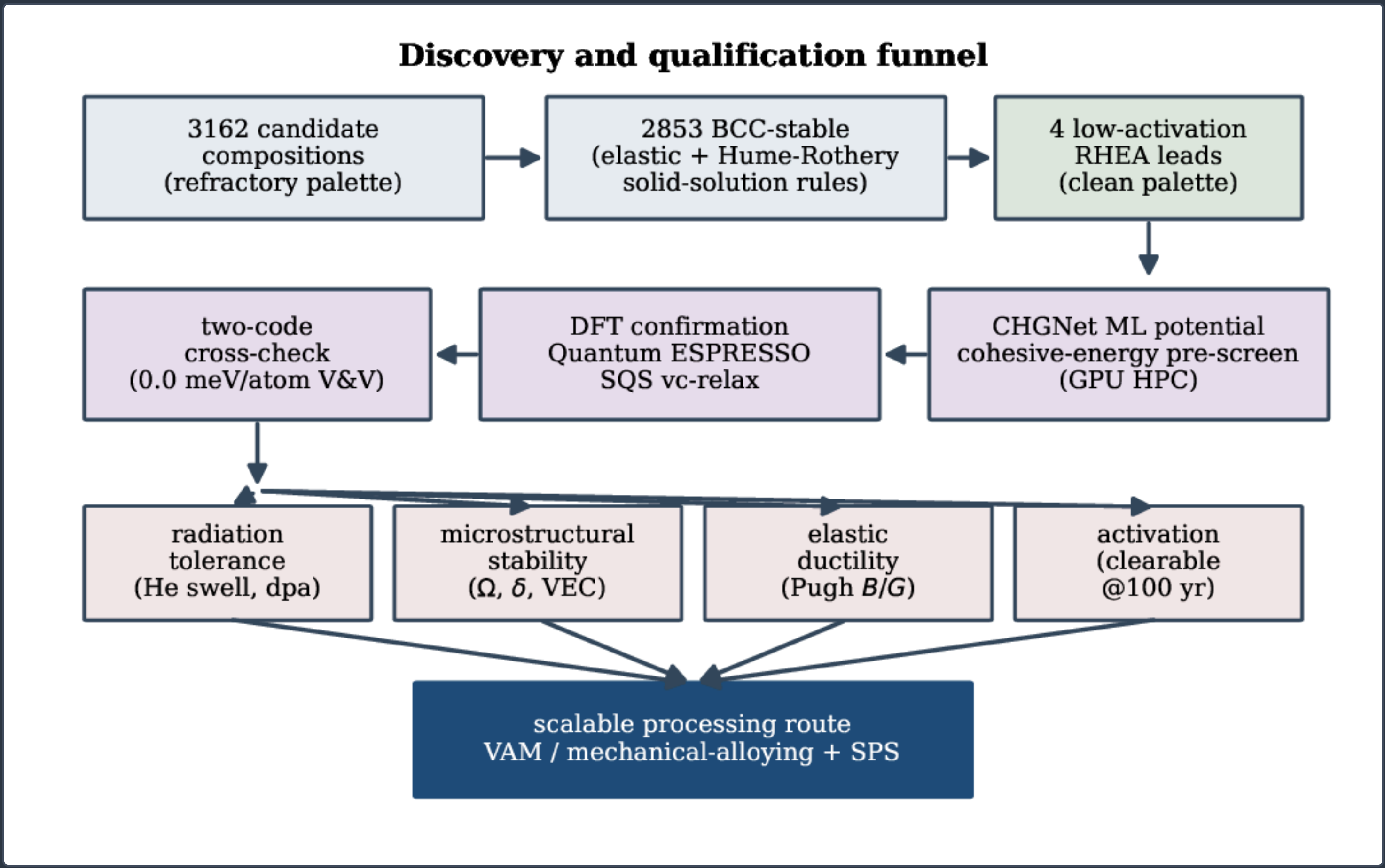

(Schematic.) The discovery-and-qualification funnel executed on the NVIDIA GPU HPC campaign: a CHGNet MLIP screen of 3162 compositions (2853 BCC-admissible) narrows to four low-activation RHEA leads; DFT on SQS with a two-code cross-check confirms the formation energies; and the service constraints of Eq. (17) — radiation tolerance, microstructural stability, ductility and activation — gate the survivor into a scalable processing route. Structure only; no data values are shown.

§ 4

Results

THE SCREEN AND THE FLAGSHIP ALLOY

The CHGNet pre-screen orders the four plasma-facing roles cleanly (figure 2); its purpose is to spend the first-principles budget only where it matters, and it correctly reproduces the top-ranked divertor candidate while flagging the near-degenerate first-wall/DEC ordering for DFT arbitration. Passing the leaders to Quantum ESPRESSO yields the flagship: the chromium-free equiatomic W–Ta–V–Ti solid solution, with a converged variable-cell formation energy of $\Delta H_f = +0.003\,\mathrm{eV/atom}$ (BR-L2-A35) and a melting point of $2777\,K$ (BR-SX-01). Chromium is excluded from the flagship deliberately: it is the constituent most prone to radiation-induced segregation and the one that most complicates the activation ledger, so removing it both simplifies the microstructure and cleans the waste class.

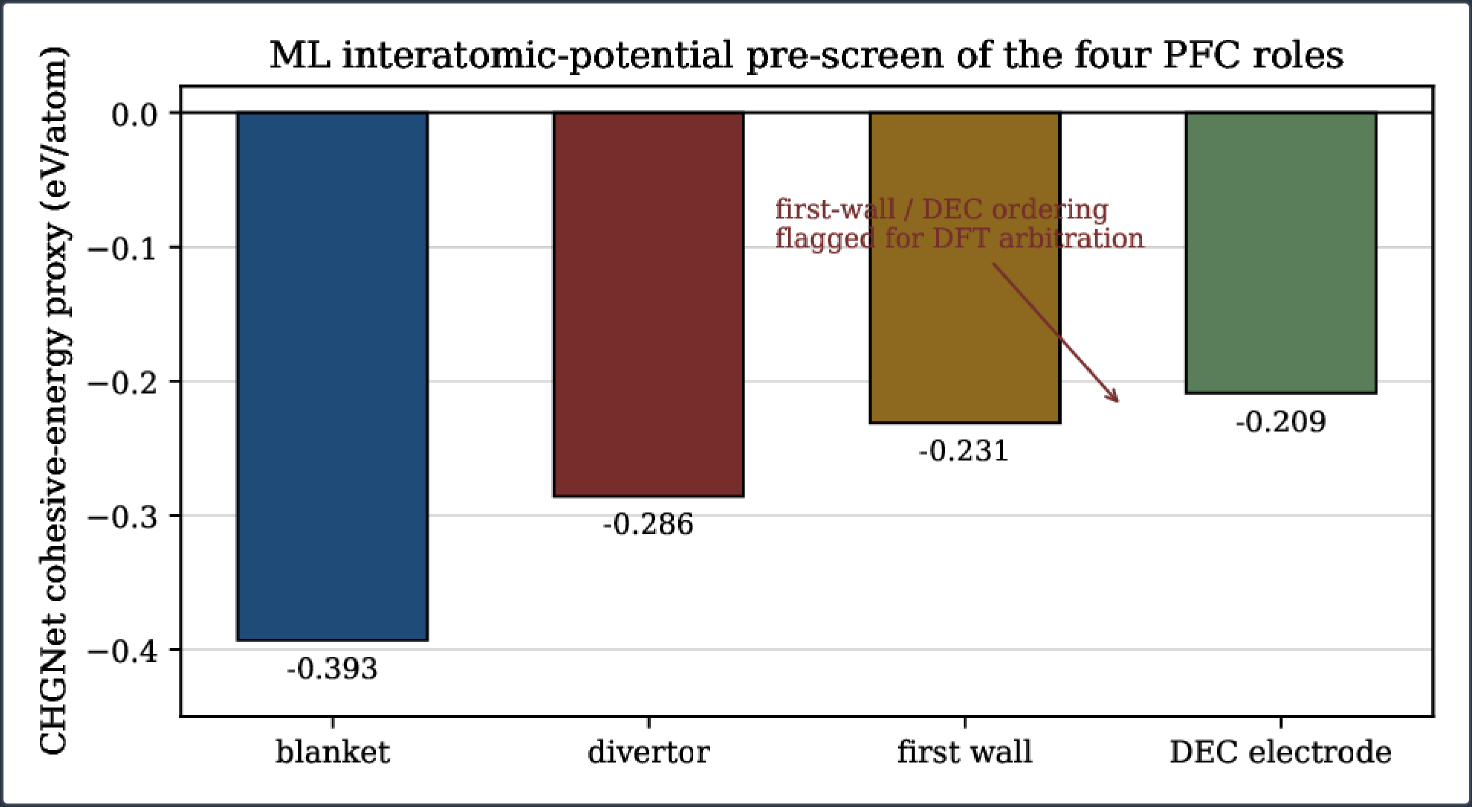

Machine-learning interatomic-potential (CHGNet) pre-screen of the four plasma-facing roles by cohesive-energy proxy (KX-L1-A4, BR-L2-A8). The screen ranks candidates cheaply before DFT; the near-degenerate first-wall/DEC ordering was flagged for DFT arbitration.

The flagship anchors a near-neutral family that covers every hot plasma-facing role, with a tantalum-bearing high-cohesion option and a fully tantalum-free option in each (table 1, figure 3). The tantalum-bearing divertor alloy $Cr_1Ta_5Ti_3V_3W_4$ relaxes to $+0.015\,\mathrm{eV/atom}$ (BR-L2-A32); the tantalum-free variants keep every role near-neutral or slightly stable — divertor $Cr_2Ti_4V_4W_6$ at -0.002, a titanium-rich ductile first-wall $Cr_1Ti_7V_4W_4$ at -0.002, and a tungsten-heaviest DEC electrode $Cr_2Ti_5V_1W_8$ at $-0.015\,\mathrm{eV/atom}$ (BR-L2-A37a–c). Every member falls inside a near-neutral band $|\Delta H_f| < 0.025\,\mathrm{eV/atom}$, and a tantalum-free path exists for every role — useful because it removes a constituent with its own activation and supply considerations, developed in full in the tantalum- and rhenium-free companion study [36].

ROLE	COMPOSITION	ΔH_f	ΔS_{mix}	δ	VEC	Ω
		(eV/at)	(J mol^{-1}K^{-1})	(%)		
refractory HEA (flagship)	W–Ta–V–Ti equiatomic	+0.003	11.53	4.05	5.00	111
divertor (high-cohesion)	$Cr_1Ta_5Ti_3V_3W_4$	+0.015	12.56	4.48	5.12	24
divertor (Ta-free)	$Cr_2Ti_4V_4W_6$	−0.002*	10.98	4.99	5.25	—
first-wall (Ta-free, ductile)	$Cr_1Ti_7V_4W_4$	−0.002*	10.21	5.10	4.88	—
DEC electrode (Ta-free)	$Cr_2Ti_5V_1W_8$	−0.015*	9.51	4.91	5.31	—
first-wall (Ta-bearing)	$Cr_1Ta_4Ti_5V_3W_3$	+0.007	12.56	4.73	4.94	52
blanket structural	$Cr_3Ta_3Ti_3V_3W_4$	+0.021	13.32	5.45	5.25	18

The refractory HEA family: composition, DFT formation energy, and the derived microstructural-stability descriptors of Eqs. (1), (4)–(5) and (3). Ω is evaluated at $=§I2777

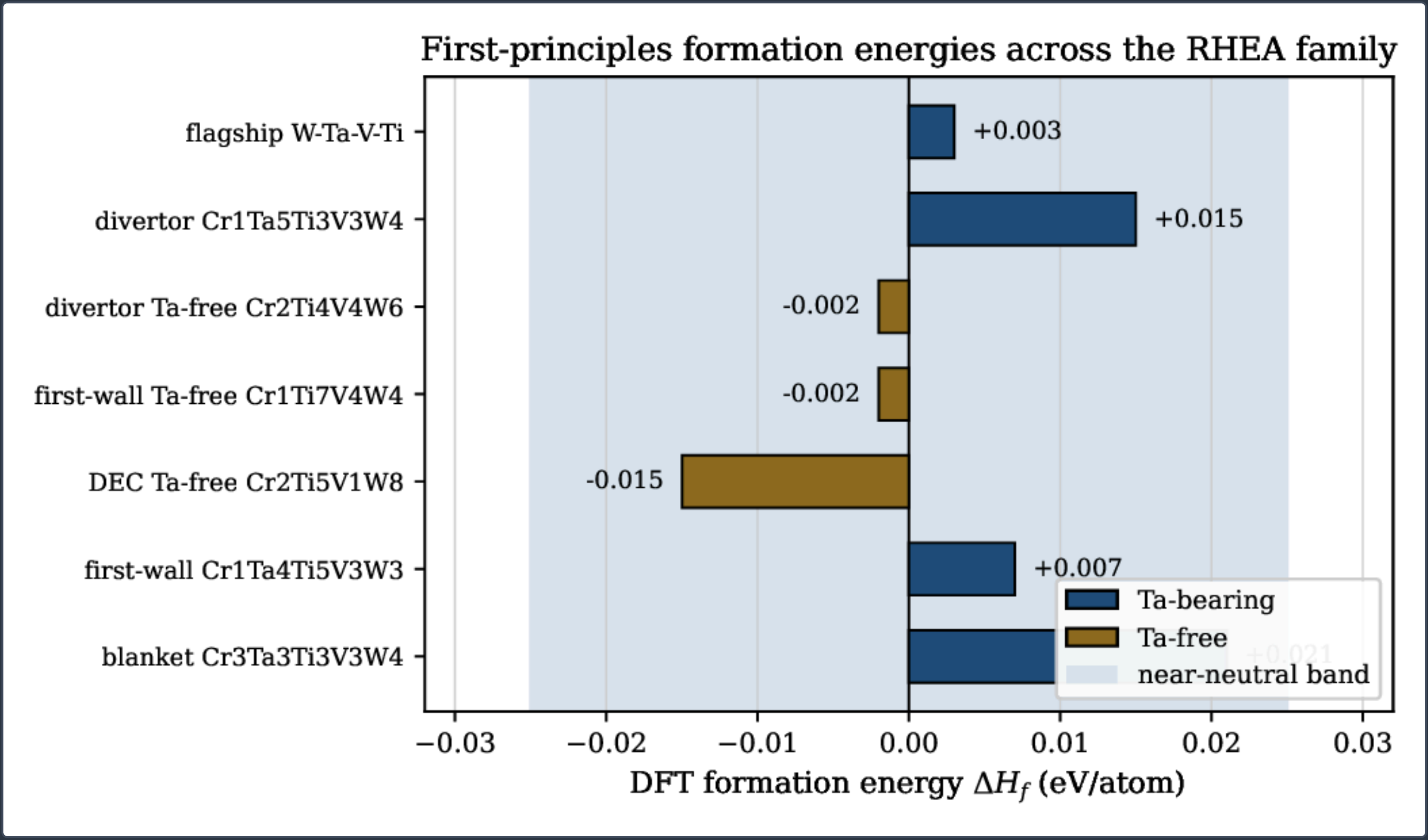

DFT formation energies across the refractory HEA family (BR-L2-A35, A32, A37a–c, A34, A31). All members fall inside the near-neutral band $|\Delta H_f| < 0.025\,\mathrm{eV/atom}$ (shaded), with a tantalum-free option (ochre) for the divertor, first-wall and DEC-electrode roles alongside the tantalum-bearing flagship and divertor alloys (blue).

MICROSTRUCTURAL STABILITY: WHY THE SINGLE PHASE HOLDS

Table 1 makes the stability case quantitative through the model of §2. Every member sits inside the Hume-Rothery single-phase-BCC window — atomic-size mismatch δ between 4.05% and 5.45% (all below the 6.6% limit) and valence-electron concentration between 4.88 and 5.31 (all below the 6.87 BCC/FCC boundary) — as figure 4 shows. The entropy-stabilization ratio of Eq. (3) is the decisive number for the enthalpy-positive members: because the DFT formation energies are near-neutral, Ω ranges from 18 (blanket quinary) through 52 (Ta-bearing first-wall) to 111 for the flagship (figure 4) — one to two orders of magnitude above the $\Omega \geq 1.1$ single-phase threshold. The physical reading is direct: the mixing enthalpy is so small that the configurational-entropy term $-T\Delta S_{\text{mix}}$ dominates the free energy of Eq. (2) by a wide margin at any relevant operating temperature, which is exactly what “entropy-stabilized” means and exactly why a near-neutral ΔH_f is the target rather than a concern. The three enthalpy-negative Ta-free members are additionally stable on enthalpy alone.

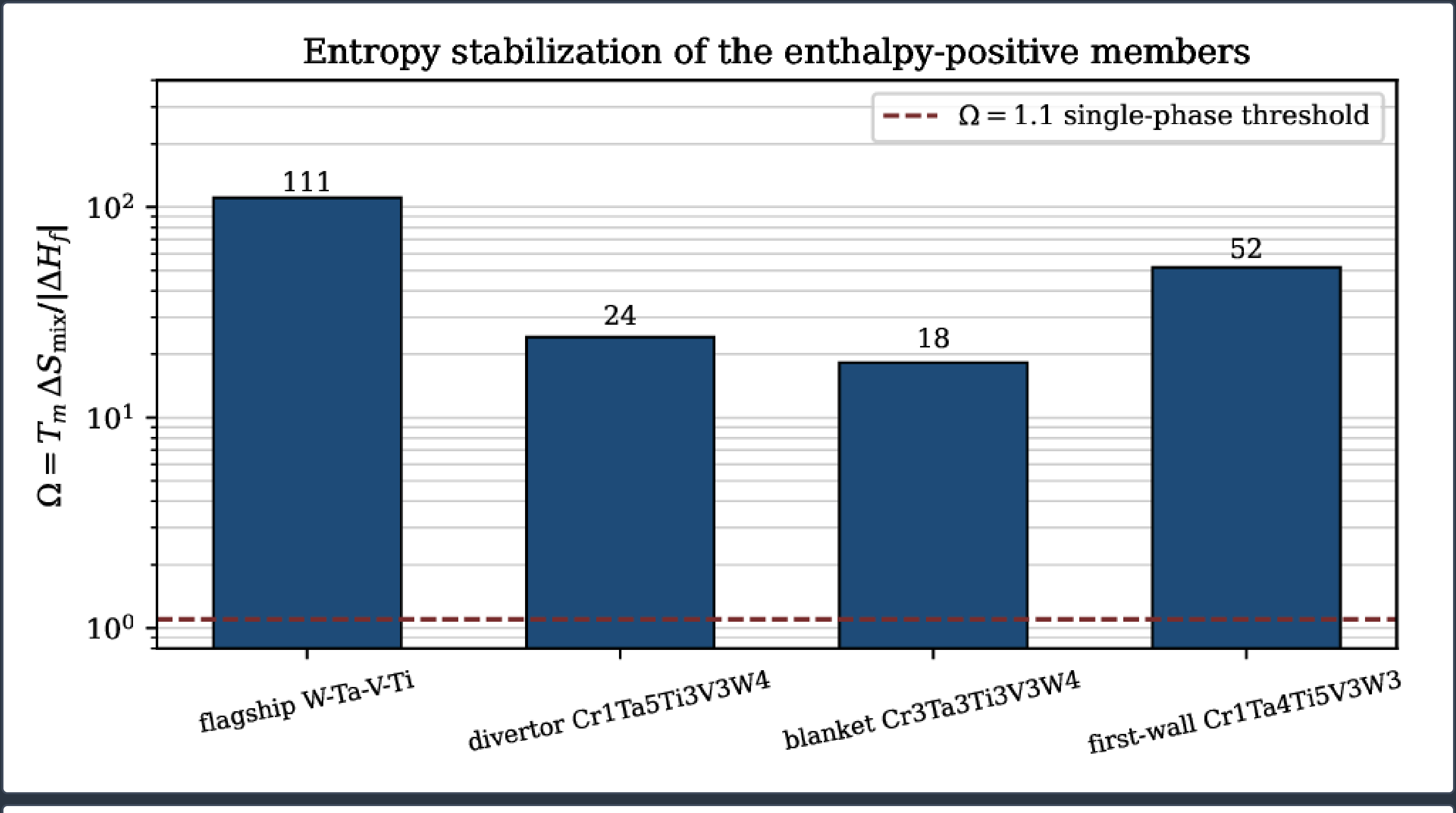

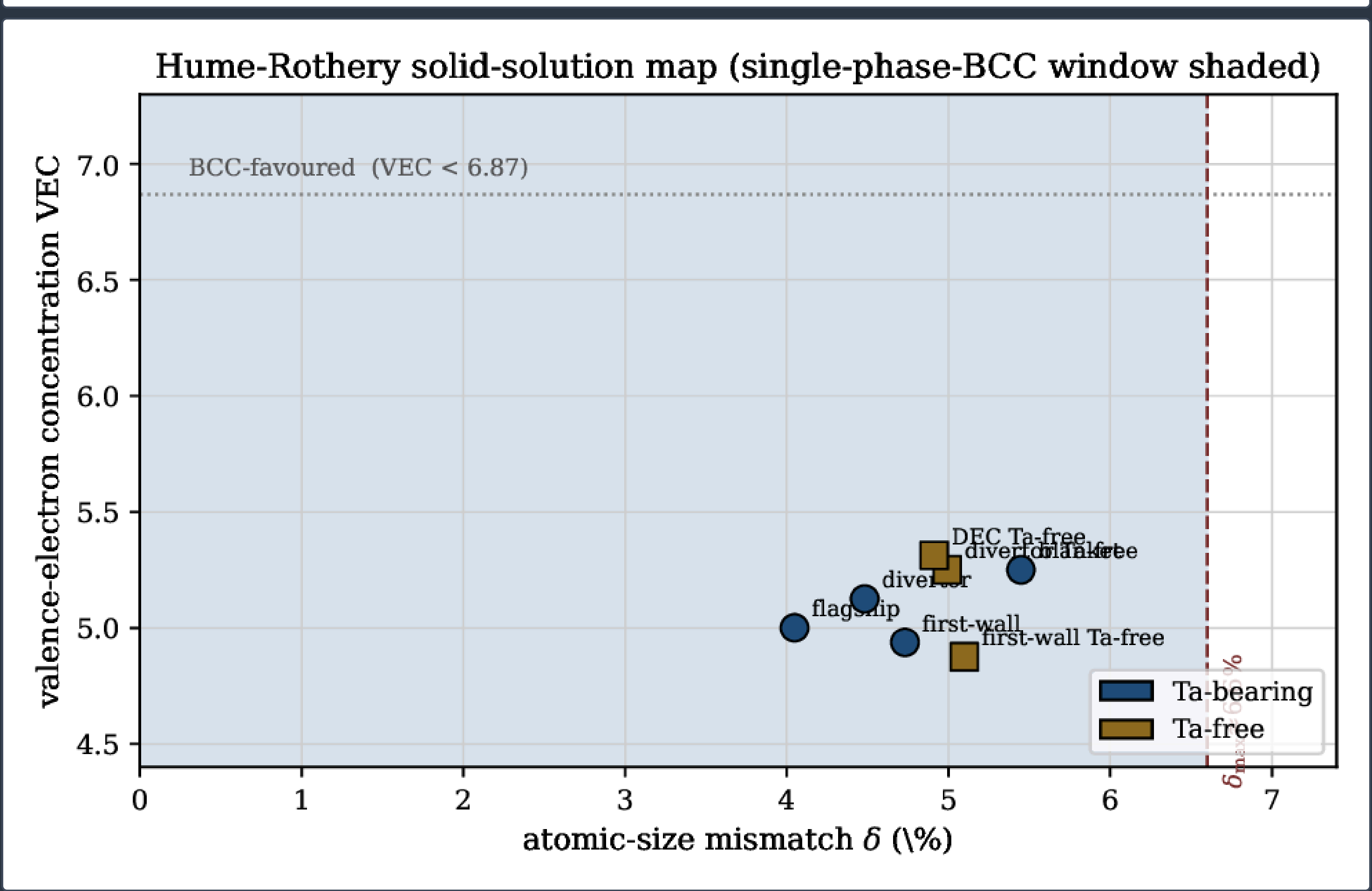

Entropy-stabilization ratio $\Omega = T_{\mathrm{m}}\Delta S_{\mathrm{mix}}/|\Delta H_f|$ (Eq. 3) for the enthalpy-positive members, evaluated at $T_{\mathrm{m}} = 2777\,K$. All exceed the $\Omega = 1.1$ single-phase threshold (dashed) by one-to-two orders of magnitude because the DFT enthalpy is near-neutral. Logarithmic axis.

Mechanical stability closes the microstructural case. A reduced-order elastic screen finds every screened composition (FeCrV, FeCrVW, RAFM, WTaVFe) Born-stable under Eq. (9) and ductile by the Pugh criterion, with $B/G \in [1.83, 2.22]$ — comfortably above the 1.75 ductile/brittle line (figure 5; BR-SX-05). The alloy is therefore not a brittle refractory but a workable one, which is what makes the processing route of §5 credible. (The full DFT elastic tensor C_{ij} is deferred to a dedicated calculation; see §7.)

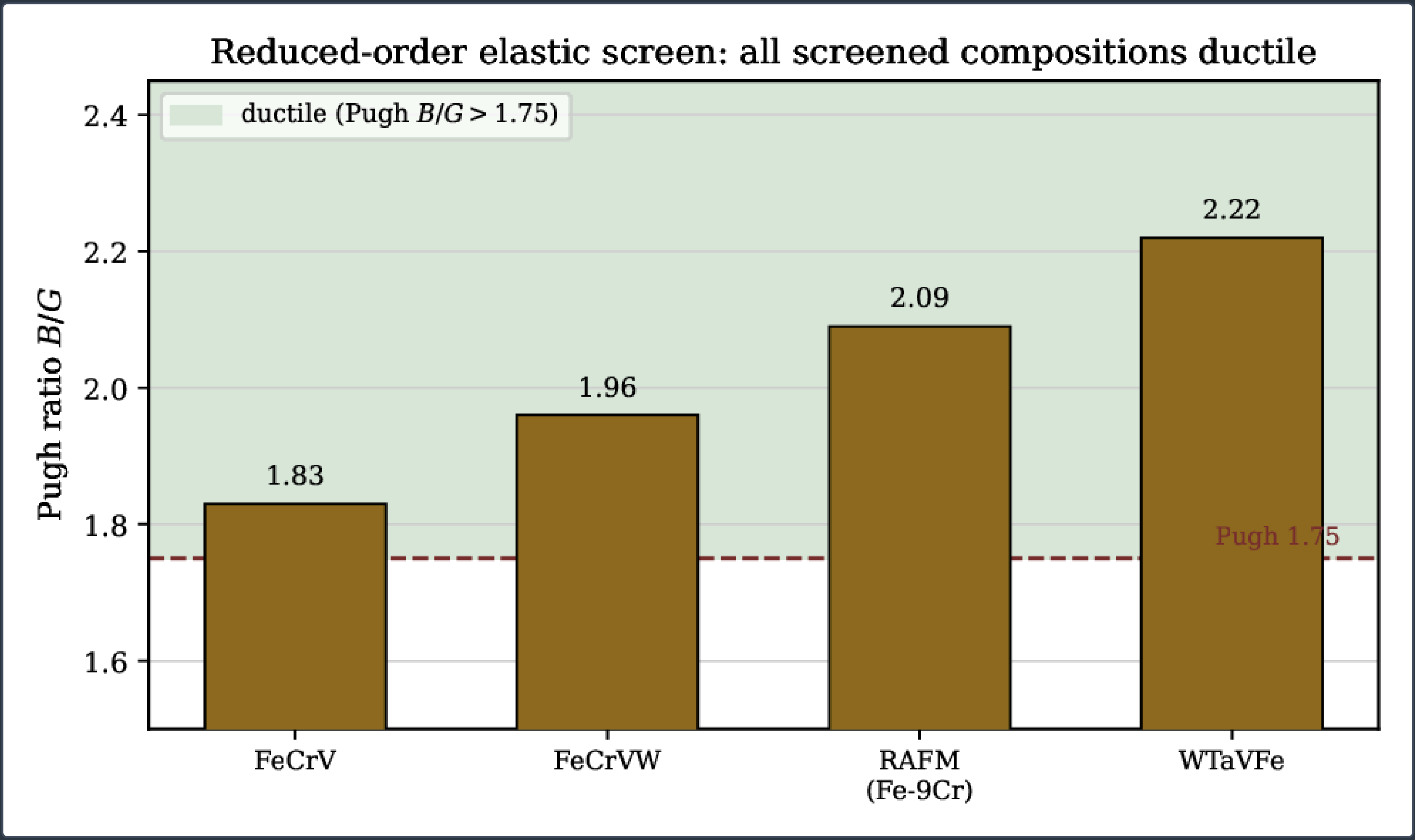

Reduced-order elastic screen (BR-SX-05): the Pugh ratio B/G of the four Born-stable screened compositions all lie in the ductile region above the $B/G = 1.75$ line (dashed). Values span the reported range $[1.83, 2.22]$; the per-composition split within that band is illustrative of the reported range.

RADIATION TOLERANCE

The alloy meets the two first-order irradiation concerns. *Helium swelling.* Evaluating Eq. (16) at the rate-theory bubble population $(\bar{r}, N_b) = (0.63\,nm,\ 2.3e23\,/cubicm)$ gives a volumetric swelling of 0.024% in tungsten at **226 appm** helium per fpy, and 0.017% in a ferritic (Fe-9Cr) comparator — both far below the 1–5% plasma-facing swelling limit and both corroborated by an independent fleet kinetic-Monte-Carlo run (BR-L2-A26). Figure 6 plots the register anchors together with the conservative linear-in-dose upper bound of Eqs. (14)–(16): even carried to five full-power-years of retained helium the swelling stays an order of magnitude under the limit. Swelling is therefore not life-limiting on the evidence in hand.

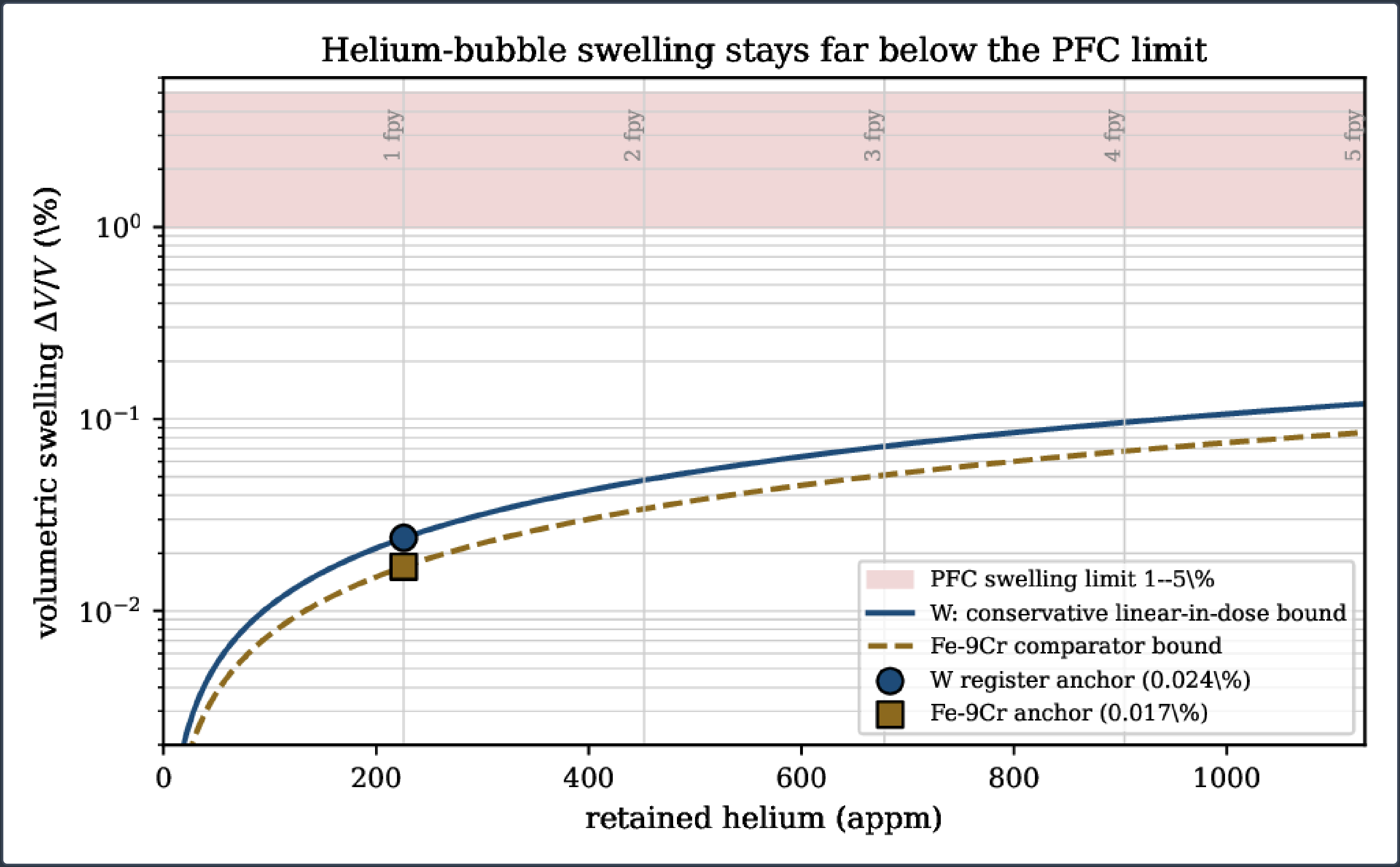

Helium-bubble swelling (Eq. 16) versus retained helium. Register anchors (BR-L2-A26): tungsten 0.024% and Fe-9Cr 0.017% at **226 appm** He fpy^{-1}. Lines are the conservative linear-in-dose upper bound; the shaded band is the 1–5% plasma-facing swelling limit. Logarithmic swelling axis.

Displacement production. The heavy-Z, chemically disordered lattice is intrinsically damage-lean. The larger threshold displacement energy of tungsten enters Eq. (11) directly: a $15\,keV$ cascade produces only 52.7 NRT displacements in tungsten against 108.8 in iron (BR-L2-A24; figure 7), and the arc-dpa correction of Eq. (12) — together with the disorder-shortened defect lifetimes established for concentrated alloys [12,13] — reduces the surviving-defect count further. The first-wall damage rate that the alloy must tolerate, **18.85–19.66 dpa/fpy** from Eq. (13) (BR-L1-A13, BR-SX-02), sets the replacement cadence rather than a swelling failure; damage lifetime and erosion are treated in the companion first-wall studies [38].

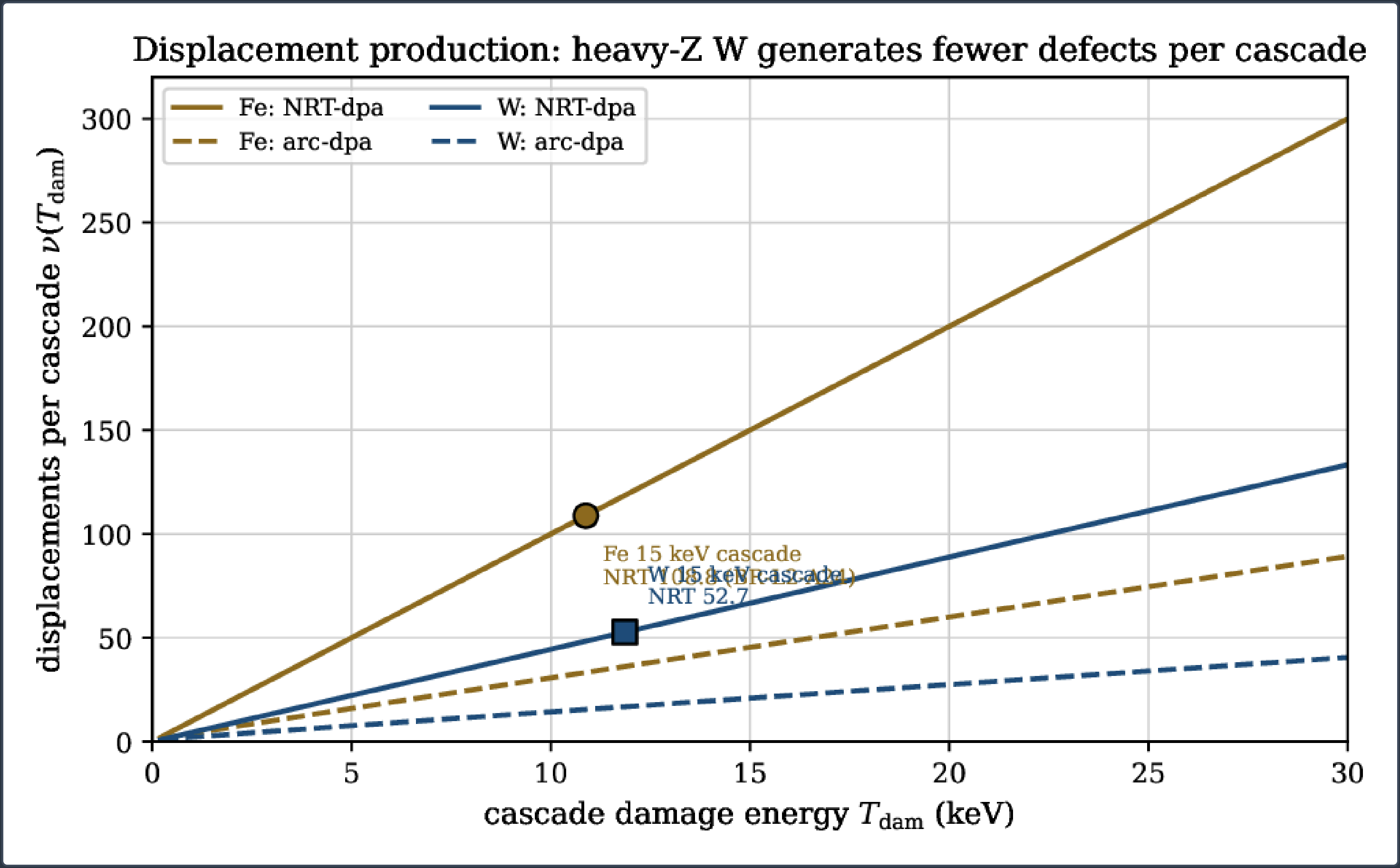

NRT (Eq. 11) and arc-dpa (Eq. 12) displacement functions versus cascade damage energy for tungsten and iron. Markers are the 15 keV-cascade register anchors: 52.7 displacements in tungsten, 108.8 in iron (BR-L2-A24). The heavier tungsten produces fewer defects per cascade.

ACTIVATION

The clean {W,Ta,V,Ti,Cr} palette is chosen so that the alloy activates only into short-lived isotopes. A full-chain ALARA/OpenMC depletion at the **85.04 MW** source finds every component at or below Class C with no greater-than-Class-C waste, and the plasma-facing HEA decays through the waste classes with a long-lived fraction of zero — ILW^{+} at one year, low-level waste by ten years, and clearable by one hundred (BR-L1-A10, ENV-A2). The contrast with a niobium/zirconium/molybdenum-bearing refractory HEA, which carries a long-lived $^{94}Nb/^{93}Zr$ tail and stays ILW^{+} indefinitely, is the entire reason the palette is restricted (figure 8). The activation, waste-routing and decommissioning case is developed in full in the companion activation study [39].

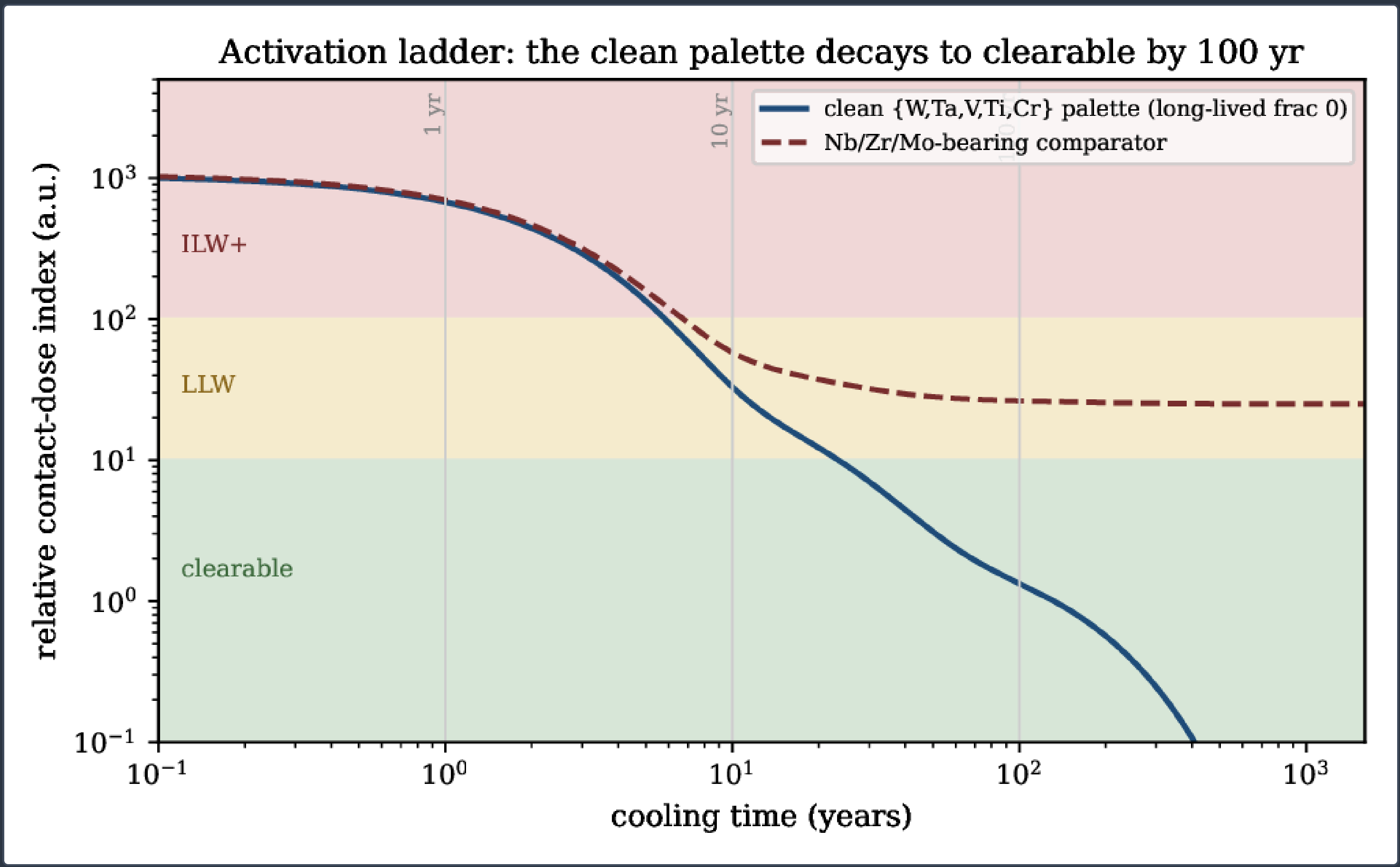

Activation ladder (BR-L1-A10, ENV-A2): the clean-palette alloy (blue) decays through the waste classes to clearable by 100 with a long-lived fraction of zero, whereas a Nb/Zr/Mo-bearing comparator (red, dashed) plateaus at ILW^{+}. Relative contact-dose index; class thresholds illustrative.

§ 5

A scalable processing route

A plasma-facing alloy is only useful if it can be made in fusion-relevant quantities and shapes. The ductility result above (Pugh $B/G \geq 1.83$) is what makes conventional metalworking of this refractory solid solution credible, and two consolidation routes are available (figure 9). *Route A — melt metallurgy.* Repeated vacuum arc melting of the elemental charge produces a homogeneous ingot; a homogenization anneal at 1400–1600 $^{\circ}C$ removes the as-cast dendritic segregation characteristic of refractory HEAs [4], and hot rolling or extrusion followed by a recrystallization anneal yields the single-phase BCC product. *Route B — powder metallurgy.* Gas-atomized or mechanically alloyed elemental powders are consolidated by spark-plasma sintering (SPS) at 1500–1700 $^{\circ}C$ into near-net-shape plasma-facing tiles. The powder route is not speculative for this alloy class: Waseem and Ryu demonstrated powder-metallurgy processing of a fusion-oriented W_xTaTiVCr high-entropy alloy and its derivatives [32], and powder-metallurgy manufacture of HEAs is an established field [33]. Both routes converge on qualification coupons for XRD single-phase confirmation and irradiation, which is the confirming measurement discussed in §7. The register's own composition-of-matter framing is that the clean-palette RHEA is manufacturable by exactly these routes; the present paper supplies the stability and radiation-tolerance physics that justifies committing to them.

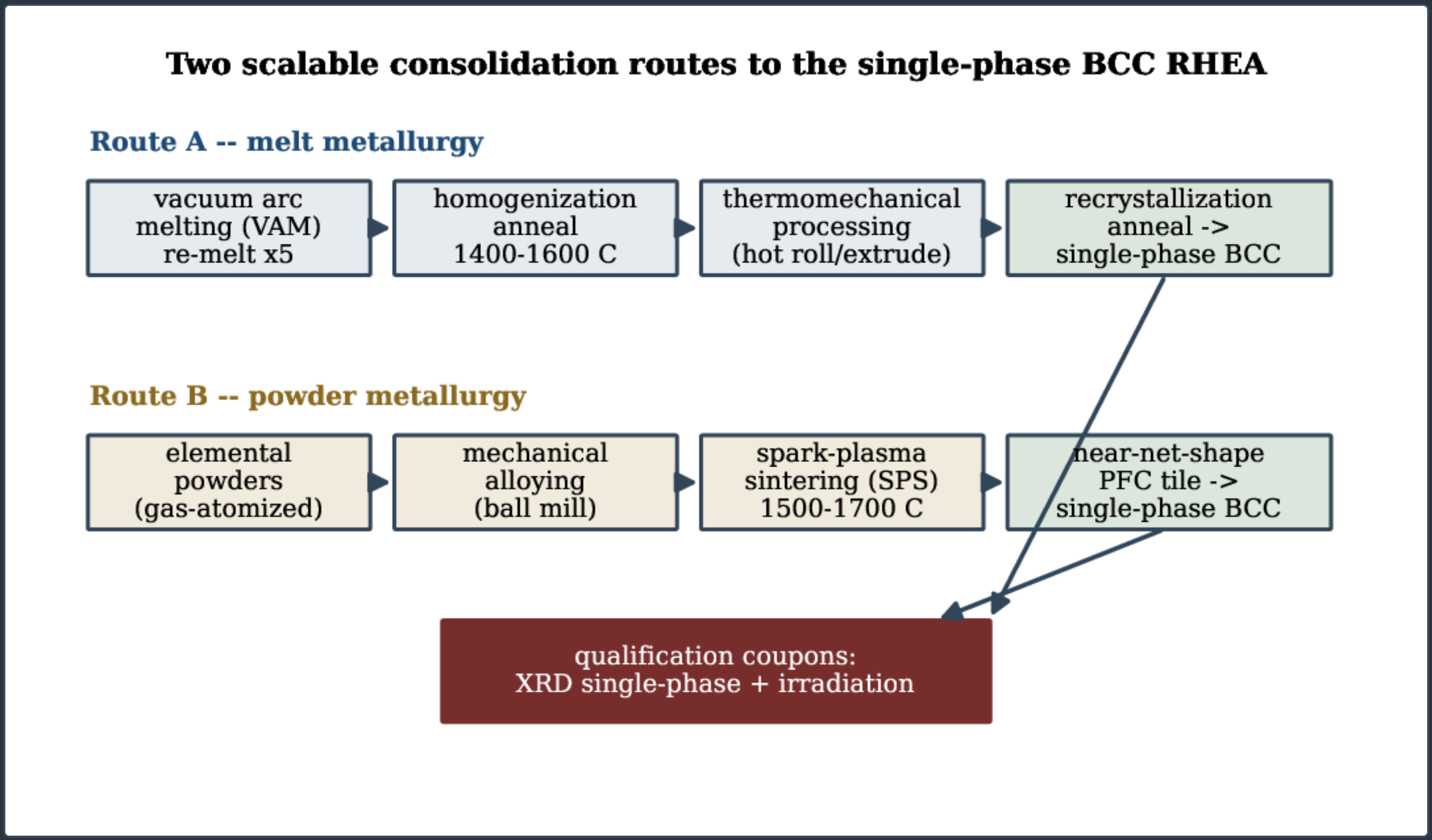

(Schematic.) Two scalable consolidation routes to the single-phase BCC RHEA plasma-facing component: Route A (vacuum arc melting → homogenization → thermomechanical processing → recrystallization) and Route B (elemental powders → mechanical alloying → spark-plasma sintering → near-net-shape tile), converging on single-phase and irradiation qualification coupons. Structure only; no data values are shown.

§ 6

Discussion

AGAINST THE RADIATION-TOLERANCE LITERATURE

The central claim — that a tungsten-based refractory HEA can absorb fusion neutron damage without swelling — is consistent with, and quantitatively bounded by, the published record. El-Atwani *et al.* measured *outstanding* radiation resistance in a WTaCrV refractory HEA, finding nanoscale dislocation loops and no detectable void swelling under heavy-ion irradiation [14]; the mechanism they identify — sluggish, disorder-limited defect transport that keeps clusters small — is the same mechanism established for concentrated single-phase alloys by Granberg [12] and Lu [13], and it is precisely what our reaction-rate result of 0.024% swelling (Eq. 16, BR-L2-A26) reflects: a dense population of $\sim 0.6\,\mathrm{nm}$ bubbles that never coarsen into voids. Our contribution is not to re-establish that refractory HEAs are radiation-tolerant but to identify a *specific, low-activation, ductile* member of that class, with the single-phase stability made quantitative through $\Omega \approx 111$ and the swelling and displacement numbers tied to the actual Hyperion neutron environment.

AGAINST THE PHASE-STABILITY RULES

The microstructural-stability descriptors of table 1 place the alloy squarely inside the empirical single-phase-solid-solution window established across the HEA literature: $\delta < 6.6\%$ and a BCC-favouring $\mathrm{VEC} < 6.87$ [8,9], with an entropy-stabilization ratio [1] far above threshold. Where our treatment differs from the conventional rule application is that we do not estimate the mixing enthalpy from tabulated Miedema binaries but take it from the same first-principles SQS calculation that validates the composition (Eqs. 8, 3); the near-neutral DFT enthalpy is what drives Ω to $\mathcal{O}(10^2)$ and removes the ambiguity that binary-enthalpy estimates carry for a five-metal system. This makes the stability statement an output of the electronic-structure calculation rather than a separate empirical overlay.

AGAINST THE TUNGSTEN AND RAFM BASELINES

Relative to monolithic tungsten, the RHEA trades a small reduction in melting point (the flagship's $2777\,K$ against tungsten's $3695\,K$) for ductility (Pugh $B/G \geq 1.83$ against tungsten's brittle $B/G \approx 1.4$) and for the disorder-driven radiation tolerance above; relative to RAFM steel [16], it trades weldability for a far higher operating-temperature ceiling and the sputter resistance of a tungsten-rich surface. The clean-palette activation ladder (figure 8) matches the reduced-activation intent of both baselines while extending it across all four plasma-facing roles [35,36]. The alloy is thus positioned not as a replacement for either baseline everywhere, but as the single solid solution that meets the compact breeder's combined strength-, radiation-, and activation-constraints where neither baseline does alone.

§ 7

Limitations

One honest gate bounds the claims. The formation energies are near-neutral — marginally positive for the tantalum-bearing members — so thermodynamic stability rests on the finite-temperature entropy term of Eq. (2) rather than on a strongly negative enthalpy; the single-phase claim is therefore a free-energy argument (Eq. 3) that a dense-mesh DFT refinement is confirming to the final digit, and the full DFT elastic tensor C_{ij} that would replace the reduced-order Pugh screen is deferred to a dedicated calculation. The confirming measurement is experimental: synthesized coupons with XRD single-phase verification and post-irradiation examination of swelling and mechanical properties, along the processing routes of §5. Until those coupons exist the alloy is a computationally grounded design, not a qualified material; the value of the present work is that it makes the target composition, its stability physics, and its manufacturing route explicit enough to test.

§ 8

Conclusion

A machine-learning-screened, DFT-validated refractory high-entropy alloy — the chromium-free equiatomic W–Ta–V–Ti solid solution — meets the compact breeder's combined plasma-facing constraints. Its formation energy of $+0.003\,\mathrm{eV/atom}$ is near-neutral by design, and the microstructural-stability physics is quantitative: a configurational entropy of $R\ln 4$, an atomic-size mismatch of 4.1% and a valence-electron concentration of 5.0 place it inside the single-phase-BCC window, and an entropy-stabilization ratio of $\Omega \approx 111$ shows the single phase is favoured by two orders of magnitude. Radiation tolerance is favourable on independent measures — 0.024% helium-bubble swelling at $226\,\mathrm{appm}$ He fpy^{-1}, far below the plasma-facing limit, and a damage-lean 52.7-displacement tungsten cascade — and the clean palette decays to a clearable waste class within a century with a long-lived fraction of zero. A reduced-order elastic screen finds the alloy ductile ($B/G \geq 1.83$), and two scalable consolidation routes, melt-metallurgical and powder-metallurgical, carry it from composition to coupon. The alloy is a coherent, computationally grounded, radiation-tolerant materials basis for the breeder's hot surfaces, anchoring a near-neutral, tantalum-optional family across all four plasma-facing roles.

Acknowledgments tocsectionAcknowledgments Part of the Kronos Fusion Energy 2026 design series. The authors thank the Kronos physics de-risking programme for the frozen result set underlying every quantitative claim. All electronic-structure, interatomic-potential and radiation-damage computation was performed on the NVIDIA GPU HPC campaign.

Reproducibility. The alloy formation energies (flagship $+0.003$; divertor $+0.015/-0.002$; first-wall $-0.002/+0.007$; DEC $-0.015\,\mathrm{eV/atom}$), the derived stability descriptors (ΔS_{mix}, δ, VEC, Ω), the helium-swelling estimate ($0.024\%/0.017\%$), the displacement counts ($52.7/108.8$), the elastic B/G band and the activation ladder are frozen gates in the Kronos Physics De-Risking Register (BR-L2-A35, A32, A9, A37a–c, A31, A34, A26, A24, BR-SX-01, BR-SX-05, BR-L1-A10, ENV-A2) and are regenerable from the archived DFT inputs (special quasi-random structures, PBE pseudopotentials, k-meshes) and the deposited figure scripts. This paper is archived at doi:10.5281/zenodo.22645868; official version: https://www.kronosfusionenergy.com/publications/a-radiation-tolerant-refractory-high-entropy-alloy-for-.html and its official version is at https://www.kronosfusionenergy.com/publications/a-radiation-tolerant-refractory-high-entropy-alloy-for-.html; the de-risking register is at doi:10.5281/zenodo.22133057.

Data availability tocsectionData availability This paper is archived at doi:10.5281/zenodo.22645868. The CHGNet screen, the SQS and DFT input decks, the radiation-damage-chain inputs and the formation-energy and figure-generation scripts are archived with the deposit and reference the Kronos 2026 series. All quantitative values trace to the register [34] by the serial identifiers cited inline. Any economic analysis is reported separately and is not included in the public deposit.

Competing interests tocsectionCompeting interests Provisional patent applications relating to aspects of this work (composition-of-matter for the low-activation refractory HEA family) have been filed.

tocsectionReferences

APPARATUS

Portfolio, People & Record

The intellectual-property estate, the people who built it, the limitations that gate it, and the sources it rests on.

1	4	40	27
GRANTED PATENT	2026 PROVISIONALS	TEAM MEMBERS	2022 PROVISIONALS

INTELLECTUAL PROPERTY

The patent portfolio

The estate spans a granted high-field magnet patent, pending utility and 2026 provisional filings that map to the two products, a digital-twin control provisional, a registered trademark application, and the original 2022 provisional family. Every patentable disclosure in the five-paper arXiv drop was protected **before** publication: the breeder and burner provisionals were filed 1–2 August, and a publication-gap omnibus filing the evening before the drop swept up the DEC, plasma-control, and REBCO-winding matter of the three otherwise-unprotected papers. Patent numbers and application serials are matters of public record; claim scope is summarised, not reproduced.

GRANTED & PENDING UTILITY

US 12,009,112	High-field tilted graded-REBCO magnet architecture (KRONO-002A) · *app. 17/878,550*	GRANTED
US 17/878,507	Core device / method (KRONO-001A) · *utility*	PENDING

2026 PROVISIONAL FILINGS — MAPPED TO THE PRODUCTS

64/124,209	Hyperion — spherical-tokamak tritium / helium-3 foundry · *breeder · filed Aug 2026*	FILED
64/124,220	Aegis / MetroVolt — synchrotron-cutoff, fuel-selection & plug-winding · *generator · filed Aug 2026*	FILED
64/115,167	KRONOS-CTRL digital-twin plant control · *provisional · filed Jul 2026*	FILED
64/005,440	Integrated spherical-tokamak fusion architecture · *early integrated-architecture filing · filed Mar 2026*	FILED
64/105,530	Negative-triangularity spherical-tokamak architecture · *foundational ST filing · filed Jul 2026*	FILED
64/128,097	Publication-gap omnibus — quasineutral two-species expander DEC · provenance-gated / latency-split plasma control · as-built high-field winding & conductor architecture · *filed 7 Aug 2026, the evening before the arXiv drop*	FILED

TRADEMARK & ORIGIN

FTK-98801894	Kronos Fusion Energy — trademark application	FILED
KR-2022-*	Original provisional family (KR-2022-00001 … 00027) · *27 filings, 2022*	PRIORITY

The narrow, defensible magnet novelty — the specific conductor and the digital-twin winding optimisation, not high-field REBCO as a category — is the commercial core that can earn ahead of any Q > 1 milestone, with markets in fusion magnet supply, MRI/NMR, accelerators, and proton therapy. The claim is scoped honestly: the high field is a *system field* result, not a stand-alone-coil record; the small-bore plug coil is structurally infeasible as a bare winding but resolved by a stress-managed structural shield (feasible-pending-FEA); and the winding-tape experiment returned a *null result*. The value is the method, not a field record.

THE TEAM

Founding partners, board, advisors & auditors

Kronos is built by a bench of advanced-fuel-fusion, high-field-magnet, direct-conversion, and materials specialists, with a board and operations team drawn from defense, national laboratories, and industry. Dates are shown as ranges; where a tenure has ended or is term-ending, the range says so.

FOUNDING PARTNERS — SCIENCE

Dr. Gerald Kulcinski
Co-Founder · Helium-3 & Advanced-Fuel Fusion
UW–Madison · 2023–Present

Dr. Carl Weggel
Chief Scientist / S.M.A.R.T. Design
MIT Alcator Program · 2022–Present

Dr. Robert J. Weggel
Magnetic Field Design
MIT Magnet Lab · 2022–Present

BOARD

Priyanca Ford
Founder & CEO · Executive Board
2022–Present

Bandel Carano
Finance / Strategy
Oak Investment Partners / Stanford · 2025–2026

Patrick Schweiger
Fusion Device Engineering
Oklo / CFS / TerraPower · 2025–Present

SCIENTIFIC ADVISORS

Dr. Steven O. Dean
Fusion Policy & History
DOE / Fusion Power Associates · 2025–Present

Dr. Patrick H. Diamond
Plasma Turbulence & Transport
UC San Diego · 2025–Present

Dr. Jack J. Dongarra
HPC & Numerical Algorithms
Turing Award · 2025–Present

Dr. Nasr M. Ghoniem
Chief Material Scientist
UCLA · 2025–Present

Dr. Siegfried Glenzer
Plasma Physics & Laser Fusion
Stanford / SLAC · 2022–Present

Dr. David A. Hammer
Pulsed-Power Fusion
Cornell · 2025–Present

Dr. Donald A. Spong
Plasma Theory & Confinement
ORNL · 2025–Present

Dr. Curtis Smith
Risk Assessment & Nuclear PRA
MIT / Idaho National Lab · 2025–Present

RADM (Ret.) David Goggins
Naval Engineering & Power-Plant Design
U.S. Navy · 2023–2026

Dr. Konstantin Batygin
Mathematician
Caltech · 2022–2025

Dr. Ruben Fair
Magnet Design / ITER Liaison
PPPL / Jefferson Lab · 2022–2025

Dr. Paul S. Weiss
Materials & Nanotechnology
UCLA · 2022–2025

SCIENTIFIC AUDITORS

Dr. Wilfred A. Cooper
Plasma Equilibrium Theory
EPFL / Swiss Plasma Center · 2025–Present

Dr. Ahmed Hassanein
Plasma–Material Interactions
Purdue / Argonne · 2025–Present

Dr. Patrick E. Hopkins
Extreme Thermal Materials
U. of Virginia · 2025–Present

Dr. Peter Hosemann
Materials Joining & Structural Integrity
UC Berkeley · 2025–Present

Dr. Travis W. Knight
Advanced Nuclear Fuels & Systems
U. of South Carolina · 2025–Present

Dr. Philippe Lebrun
Cryogenics & Magnet Cooling
CERN · 2025–Present

Dr. Nitendra Singh
Nuclear Safety & Fuel Cycle
ITER · 2025–Present

Dr. Guido Van Oost
Magnetic Confinement & Fusion Systems
Ghent University · 2025–Present

Dr. Gary S. Was
Radiation Materials & Structural Integrity
U. of Michigan · 2025–Present

Dr. Ray Sedwick
Direct Energy Conversion
U. of Maryland · 2025

OPERATIONS

Michael Laughlin
Chief Operating Officer
2022–Present

Martin Owens
Chief Strategy Officer
LANL / GE Hitachi · 2022–Present

MG (Ret.) Paul Pardew
Chief Contracting Officer
Army Contracting Command · 2022–Present

David Beck
Fusion Commercialization
U.S. Space Force · 2024–Present

Sushma Bhatia
Environmental & Legislative
Google · 2022–Present

Michael De Frenza
Technology Licensing
2023–Present

MG (Ret.) Robin L. Fontes
Cybersecurity & Defense
Army Cyber Command · 2022–Present

Vijay Gehani
Supply Chain & Components
INOX India · 2024–Present

Jon Michel Greenwood
IT & AI Infrastructure
Live Nation · 2023–Present

Brian C. O'Neill
National Security
CIA / ODNI · 2022–Present

Gen. (Ret.) Gustave F. Perna
DoD Liaison
Operation Warp Speed · 2022–2023

Andrea Romero
Marketing Lead
2022–Present

Legal counsel is retained; those roles are held on the internal roster and are not listed here.

SOURCES

References

1 J-W Yeh *et al*, Nanostructured high-entropy alloys with multiple principal elements: novel alloy design concepts and outcomes, *Adv. Eng. Mater.* **6** 299 (2004). doi:10.1002/adem.200300567

2 B Cantor, I T H Chang, P Knight and A J B Vincent, Microstructural development in equiatomic multicomponent alloys, *Mater. Sci. Eng. A* **375–377** 213 (2004). doi:10.1016/j.msea.2003.10.257

3 O N Senkov, G B Wilks, D B Miracle, C P Chuang and P K Liaw, Refractory high-entropy alloys, *Intermetallics* **18** 1758 (2010). doi:10.1016/j.intermet.2010.05.014

4 O N Senkov, D B Miracle, K J Chaput and J-P Couzinie, Development and exploration of refractory high entropy alloys — a review, *J. Mater. Res.* **33** 3092 (2018).

5 D B Miracle and O N Senkov, A critical review of high entropy alloys and related concepts, *Acta Mater.* **122** 448 (2017). doi:10.1016/j.actamat.2016.08.081

6 E P George, D Raabe and R O Ritchie, High-entropy alloys, *Nat. Rev. Mater.* **4** 515 (2019). doi:10.1038/s41578-019-0121-4

7 Y Zhang *et al*, Microstructures and properties of high-entropy alloys, *Prog. Mater. Sci.* **61** 1 (2014). doi:10.1016/j.pmatsci.2013.10.001

8 Y Zhang, Y J Zhou, J P Lin, G L Chen and P K Liaw, Solid-solution phase formation rules for multi-component alloys, *Adv. Eng. Mater.* **10** 534 (2008).

9 S Guo, C Ng, J Lu and C T Liu, Effect of valence electron concentration on stability of fcc or bcc phase in high entropy alloys, *J. Appl. Phys.* **109** 103505 (2011).

10 M C Troparevsky, J R Morris, P R C Kent, A R Lupini and G M Stocks, Criteria for predicting the formation of single-phase high-entropy alloys, *Phys. Rev. X* **5** 011041 (2015). doi:10.1103/PhysRevX.5.011041

11 Y Zhang *et al*, Influence of chemical disorder on energy dissipation and defect evolution in concentrated solid solution alloys, *Nat. Commun.* **6** 8736 (2015). doi:10.1038/ncomms9736

12 F Granberg *et al*, Mechanism of radiation damage reduction in equiatomic multicomponent single phase alloys, *Phys. Rev. Lett.* **116** 135504 (2016). doi:10.1103/PhysRevLett.116.135504

13 C Lu *et al*, Enhancing radiation tolerance by controlling defect mobility and migration pathways in multicomponent single-phase alloys, *Nat. Commun.* **7** 13564 (2016). doi:10.1038/ncomms13564

14 O El-Atwani *et al*, Outstanding radiation resistance of tungsten-based high-entropy alloys, *Sci. Adv.* **5** eaav2002 (2019). doi:10.1126/sciadv.aav2002

15 M Rieth *et al*, Recent progress in research on tungsten materials for nuclear fusion applications in Europe, *J. Nucl. Mater.* **432** 482 (2013).

16 R L Klueh and A T Nelson, Ferritic/martensitic steels for next-generation reactors, *J. Nucl. Mater.* **371** 37 (2007).

17 S J Zinkle and N M Ghoniem, Operating temperature windows for fusion reactor structural materials, *Fusion Eng. Des.* **51–52** 55 (2000).

18 S J Zinkle and L L Snead, Designing radiation resistance in materials for fusion energy, *Annu. Rev. Mater. Res.* **44** 241 (2014). doi:10.1146/annurev-matsci-070813-113627

19 J P Perdew, K Burke and M Ernzerhof, Generalized gradient approximation made simple, *Phys. Rev. Lett.* **77** 3865 (1996). doi:10.1103/PhysRevLett.77.3865

20 P Giannozzi *et al*, QUANTUM ESPRESSO: a modular and open-source software project for quantum simulations of materials, *J. Phys.: Condens. Matter* **21** 395502 (2009). doi:10.1088/0953-8984/21/39/395502

21 G Kresse and J Furthmuller, Efficient iterative schemes for ab initio total-energy calculations using a plane-wave basis set, *Phys. Rev. B* **54** 11169 (1996). doi:10.1103/PhysRevB.54.11169

22 H J Monkhorst and J D Pack, Special points for Brillouin-zone integrations, *Phys. Rev. B* **13** 5188 (1976).

COLOPHON

How this document was made

The Kronos Fleet — Combined Editorial, 2026 is set in **Fraunces** (display), **Gelasio** (text), and **IBM Plex Mono** (data & equations), carried forward from the Kronos editorial design system.

The figures are rendered at 300 dpi from the deposited generator scripts; the document is composed as a single self-contained file with embedded fonts and imagery, paginated to US Letter, and rendered to PDF through a headless Chromium engine in matched light and dark editions.

Every headline quantity carries an evidence class; withdrawn and restated values are marked as such. Nothing herein is frozen beyond the founder-approved Tier-A set.

Explore it live — turn the interactive 3-D model, run the deposited solvers in the physics validator, and watch the companion film series.

LEGAL NOTICE

Notice, status, and distribution

Conceptual design & simulation study. This document reports a conceptual design and simulation study. It is not a construction commitment, a safety-analysis report, a regulatory filing, or an offer of securities. Forward-looking statements — schedules, costs, market sizes, and performance — are estimates subject to the limitations set out in the Simulations part and may change.

Numbers and their classes. Quantities are reported with evidence classes and case labels; modelled, assumed, and requirement-class values are identified as such and are not to be quoted without their labels.

Public edition. This edition carries the physics and design only; all financial, funding, and defense-commercial content has been removed for public distribution. The scientific text corresponds to the arXiv and journal submissions.

THE 2026 KRONOS SERIES

One programme, many papers

This editorial is one paper in the Kronos 2026 series — a real fusion company's complete, reproducible physics record for a spherical-tokamak breeder and its low-neutron D–^{3}He tandem-mirror burners. Every headline number is a frozen anchor in the Physics De-Risking Register.

Explore the whole programme: the De-Risking Register, the interactive 3-D model, and the physics validator.

KRONOS FUSION ENERGY

A Radiation-Tolerant Refractory High-Entropy Alloy for Fusion Plasma-Facing Components: Microstructural Stability and a Scalable Processing Route

A real fusion company building real machines. Explore the science, live.

Zenodo · doi:10.5281/zenodo.22645868

Read on kronosfusionenergy.com

The Physics De-Risking Register